

Modeling sublimation of ice exposed by new impacts in the martian mid-latitudes

Colin M. Dundas *, Shane Byrne

Department of Planetary Sciences, University of Arizona, Tucson, AZ 85721, United States

ARTICLE INFO

Article history:

Received 23 May 2009

Revised 26 August 2009

Accepted 8 September 2009

Available online 15 September 2009

Keywords:

Mars, Surface

Ices

Mars, Atmosphere

Impact processes

ABSTRACT

New impacts in the martian mid-latitudes have exposed near-surface ice. This ice is observed to slowly fade over timescales of months. In the present martian climate, exposed surface ice is unstable during summer months in the mid-latitudes and will sublimate. We model the sublimation of ice at five new impact sites and examine the implications of its persistence. Even with generally conservative assumptions, for most reasonable choices of parameters it is likely that over a millimeter of sublimation occurred in the period during which the ice was observed to fade. The persistence of visible ice through such sublimation suggests that the ice is relatively pure rather than pore-filling. Such ice could be analogous to the nearly pure ice observed by the Phoenix Lander in the “Dodo–Goldilocks” trench and suggests that the high ice contents reported by the Mars Odyssey Gamma Ray Spectrometer at high latitudes extend to the mid-latitudes. Our observations are consistent with a model of the martian ice table in which a layer with high volumetric ice content overlies pore-filling ice, although other structures are possible.

© 2009 Elsevier Inc. All rights reserved.

1. Introduction

Sublimation and evaporation have long been recognized as significant processes on Mars, relevant to understanding the evolution of ice and the possibility of liquid surface water. Exposed ice will sublimate at temperatures above the frost point. Ingersoll (1970) calculated the rate of mass loss from ice in a static atmosphere. A number of subsequent workers have produced more detailed models and derived estimates for sublimation rates on the martian surface under various conditions (e.g. Wallace and Sagan, 1979; Toon et al., 1980; Carr, 1990; Ivanov and Muhleman, 2000; Hecht, 2002; Taylor et al., 2006; Williams et al., 2008). In this paper, we investigate the sublimation of ice exposed by mid-latitude impacts. We describe a thermal model that incorporates the effect of sublimation, and model the ice loss history at the observed new impact sites with exposed ice.

Exposed ice has been reported in new impact craters in the northern mid-latitudes of Mars (Byrne et al., 2009) based on images from the Context Camera (CTX; Malin et al., 2007) and the High Resolution Imaging Science Experiment camera (HiRISE; McEwen et al., 2007) onboard the Mars Reconnaissance Orbiter. Ice patches a few meters across were observed on the floors or ejecta of small craters (Figs. 1 and 2). Byrne et al. compared the distribution of these craters with models of ice distribution and depth to stable buried ice, finding that ice has likely been recently stable at the sites and depths excavated. In contrast, surface ice is unsta-

ble in summer at these locations, and the ice exposures changed noticeably on timescales of a few months during martian summer (Fig. 1). The relatively warm summer temperatures drive sublimation from the ice surface.

An important question is whether the ice is pore-filling or relatively pure. High volumetric ice contents have been suggested at high latitudes based on Mars Odyssey Gamma Ray Spectrometer (GRS) data (e.g. Boynton et al., 2002). Pore-filling ice can be readily explained by vapor deposition from the atmosphere (Mellon and Jakosky, 1993), while formation of excess ice (ice exceeding the natural pore space of a soil) may require other processes (e.g. Mellon et al., 2008). If a large thickness sublimates before the ice is obscured by a lag, this would imply low dust content in the ice, although this may be influenced by atmospheric deposition or removal of dust. We compare model results with observations from HiRISE which show time sequences of change over several sites during martian summer. Finally, we discuss the model results in comparison with the observed timescales of ice persistence in order to assess the nature of the ice and the implications of its presence. We deliberately make mostly conservative assumptions in our calculations of the total sublimation in order to place an upper limit on the dust content of the ice.

2. Thermal and sublimation model

2.1. Thermal model

We use a one-dimensional layered thermal model similar to that of Kieffer et al. (1977) to investigate the temperature evolu-

* Corresponding author. Address: Department of Planetary Sciences, The University of Arizona, 1541 E. University Blvd., Tucson, AZ 85721, United States.

E-mail address: colind@pl.arizona.edu (C.M. Dundas).

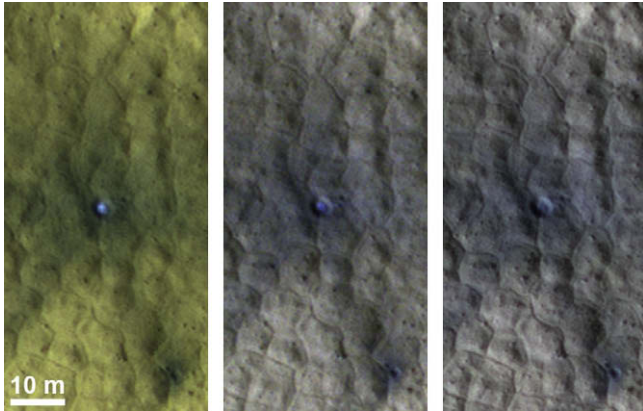


Fig. 1. HiRISE false-color images of one crater at the first ice exposure site discovered, showing visible ice at L_s 126 (September 12, 2008) and L_s 162 (November 22, 2008) but none at L_s 180. The impact occurred no later than L_s 111 (August 10, 2008), so ice remained visible for at least three and potentially up to six months. Cutouts have been stretched individually to show contrast between ice and regolith; color and brightness change in the surrounding surface is actually minimal. The ice is particularly bright in the HiRISE blue–green filter, but somewhat darker than the surroundings in the red and near-IR, and so appears blue to white in these images.

tion of the exposed ice patches. (Throughout this paper, we will refer to the exposures as ice; the dust content and ice purity are discussed in Section 5.) The model is an explicit finite-difference thermal model with layer thickness increasing geometrically with depth. We extend the model to five times the effective annual skin depth, and assume a geothermal heat flux of 30 mW m^{-2} at the base. Similar models have been used by a number of other investigators with various modifications. We solve for the energy balance of the surface layer using the following expression:

$$\frac{\partial U}{\partial t} = Q_{\text{solar}} + Q_c + Q_{\text{LWF}} - \epsilon \sigma T_{\text{surf}}^4 + SH - L_{\text{H}_2\text{O}} \frac{\partial m_{\text{sub}}}{\partial t} \quad (1)$$

where U is the energy per unit area. Q_{solar} represents the solar radiation absorbed by the surface based on the albedo and the incident solar flux. The solar flux varies with season, latitude and time of day; we use the planetographic latitude for this calculation, as this sets the incidence angle. We assume that all absorption is in the topmost model layer. Q_c represents the net conduction to or from the adjacent layers, Q_{LWF} is infrared radiation from the atmosphere and $\epsilon \sigma T^4$ is the emissivity multiplied by the blackbody radiation emitted from the surface. SH is the sensible heat imparted from the atmosphere, and the final term is the latent heat due to subli-

mation of an ice mass m_{sub} . If the surface temperature reaches the frost point of CO_2 , we hold the regolith surface temperature at the frost point and track condensation and sublimation of CO_2 ice.

The atmospheric long-wavelength flux Q_{LWF} is parameterized as emissivity multiplied by 4% of the peak noontime insolation, following Aharonson and Schorghofer (2006). Some previous models (e.g. Kieffer et al., 1977) have utilized a 2% approximation, but Haberle and Jakosky (1991) found that this is an underestimate for a clear atmosphere, and even higher values are appropriate if the atmosphere is dusty. The true flux is pressure-dependent (and therefore elevation-dependent), while this flux estimate is not; Haberle and Jakosky modeled the Viking Lander 1 site, which is at an elevation of -3.6 km , close to the elevations of the fresh craters studied here (-2.5 to -4 km), and so this should be a good approximation. This flux also varies over the diurnal cycle, and is highest in the afternoon (Haberle and Jakosky, 1991), while we assume a constant flux throughout the day and night. If this variation were incorporated, it would tend to slightly increase the amplitude of diurnal surface temperature variations and thus raise the peak temperature attained. This would slightly increase the total sublimation, since the sublimation rate depends nonlinearly on temperature. We assume a clear atmosphere at all times. Atmospheric opacity could block some incident insolation and slightly reduce the peak temperatures (Haberle and Jakosky, 1991), but northern mid-latitude optical depths in spring and summer are typically very low (Smith et al., 2001).

We set up the scenario for the impact by producing a realistic initial thermal profile using our multi-layer thermal model (Fig. 3). We considered initial conditions with two or three material layers, each comprised of many model layers. We model ice under a layer of ice-free regolith and run the model for 40 Mars years to establish a consistent initial temperature profile. Time-steps were chosen to satisfy the Courant criterion for model stability. We consider two possible scenarios at the time of impact, depending on the site morphology. If ice is exposed at the bottom of a crater, we expose the ice table by removing the regolith cover. For ice exposed in crater ejecta, we emplace ice on top of the existing model structure with ice and regolith. We omit heat deposition from the impact, which would increase the initial sublimation rates. Beginning with this stage, we also incorporate latent and sensible heat, and track sublimation of the ice from the surface.

The thermal model used in this paper is one-dimensional and assumes that all conditions are laterally uniform. Modest lateral variations probably occur, as seen at the Phoenix Lander site (Smith et al., 2009). However, for a small ice patch on a crater floor, lateral conduction of heat is likely to be a significant effect. The

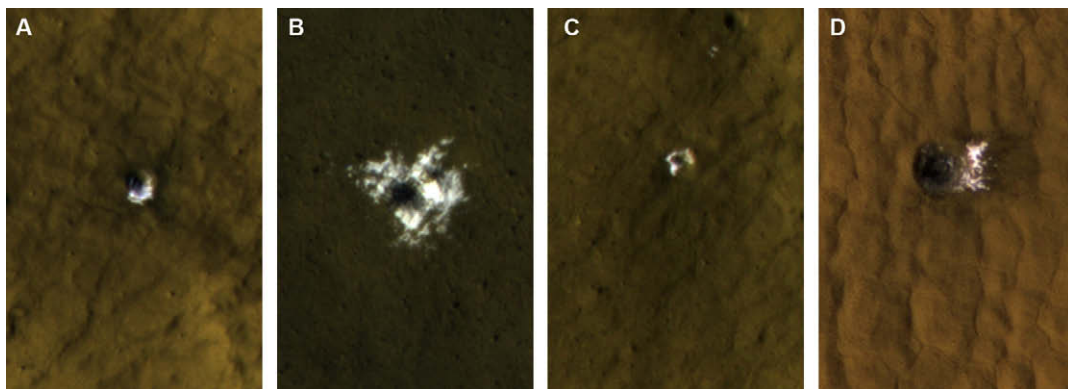


Fig. 2. HiRISE false-color images of ice exposure sites 2–5 (A–D). Each panel is 50 m wide. Each scene and each HiRISE color is individually stretched for maximum contrast. Ice appears white because it is bright in all filters, not because of the intrinsic color. (HiRISE images PSP_010440_2235, PSP_010625_2360, PSP_010585_2255 and PSP_010861_2265.)

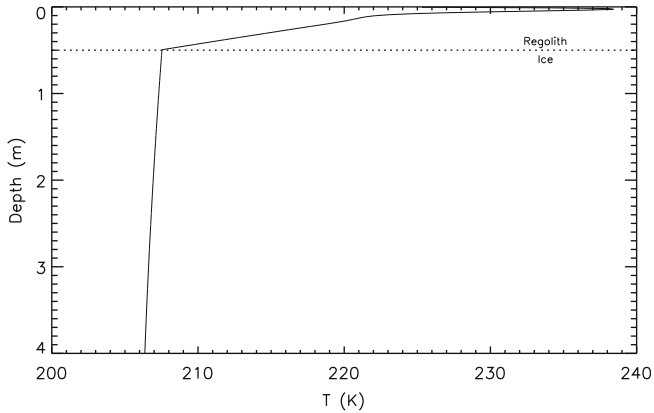


Fig. 3. Model ground temperature conditions at impact for site 1 for an assumed impact time of L_s 96. The impact is assumed to remove the ice-free regolith layer above the dotted line. Note that the excavated thickness is much larger than the diurnal skin depth, so the time of day has no effect on the temperature profile in the ice. Seasonal temperature variations propagating into the ice are resolved by the model but not visible with the truncated y-axis.

temperatures of the exposed ice are higher than the temperatures of adjacent buried ice at most times, so the buried ice acts as a net heat sink. For cases where we uncover the ice table, we estimated lateral conduction rates using the temperature difference between the exposed-ice thermal model and the temperature of the corresponding layer in a regional thermal model with the original properties, over a length scale set by the thermal diffusion length scale in ice for the time since impact. The calculated lateral fluxes were applied to change the temperature of each layer, treated as a cylinder with appropriate thickness and diameter corresponding to the approximate size of each ice patch. This approach is less accurate than a complete two-dimensional model, since the length scale for conduction is a simplistic approximation and the temperature is probably not uniform across the width of the patch, especially at depth. Furthermore, once the lateral conduction length becomes significant, vertical conduction in the material around the column will affect the lateral temperature gradients near material boundaries where the horizontal length scales differ. However, this does provide a rough estimate for lateral heat loss while retaining computational simplicity.

We omit any estimate of lateral conduction from cases where we emplace ice on top of the regolith (as in a crater ejecta blanket), because the insulating nature of the underlying regolith reduces conduction away from the surface ice and because the geometry in such cases is considerably more complex. It is still likely that there will be a thermal anomaly under the ice that will be affected by lateral conduction, and so this is not conservative with respect to sublimation. In this case the material adjacent to the ice surface will undergo significant diurnal temperature variations, and so may be a source of heat at times. The simple cylindrical symmetry assumed above is not valid for cases where one side of the ice patch is a crater wall. We do not attempt to completely model this complex situation. Instead, for comparison, we also calculate sublimation rates for an exposed ice table under identical conditions. This gives a more conservative estimate for sublimation since it includes lateral conduction and omits insulation from underlying soil.

Sensible heat flux into and out of the ice is given by the following equations (similar to Williams et al., 2008):

$$SH_{forced} = \rho_{atm} C_p A u_{wind} (T_{atm} - T_{surf}) \quad (2)$$

$$SH_{free} = 0.14 (T_{atm} - T_{surf}) k_{atm} \left(\left(\frac{C_p \mu}{k_{atm}} \right) \left(\frac{g}{v^2} \right) \left(\frac{\Delta \rho}{\rho} \right) \right)^{\frac{1}{3}} \quad (3)$$

$$SH = SH_{forced} + SH_{free}$$

Table 1
List of constants.

Constant	Description	Value
A	Drag coefficient	0.002 (dimensionless)
g	Acceleration due to gravity	3.71 m s^{-2}
k	Boltzmann's constant	$1.38066 \times 10^{-23} \text{ J K}^{-1}$
k_0	von Karman's constant	0.4 (dimensionless)
L_{H_2O}	Latent heat of sublimation for water ice	$2.83 \times 10^6 \text{ J kg}^{-1}$
M_w	Molecular mass of water	$2.99 \times 10^{-26} \text{ kg}$
m_c	Molar mass of CO_2	0.044 kg
m_w	Molar mass of water	0.018 kg
R	Universal gas constant	$8.314 \text{ J K}^{-1} \text{ mol}^{-1}$
z	Height of measurement of wind speed	1.6 m^a
ϵ	Emissivity	0.95 (dimensionless)
σ	Stefan-Boltzmann constant	$5.67 \times 10^{-8} \text{ W m}^{-2} \text{ K}^{-4}$

^a Appropriate for Viking 2 wind speed measurements (Hess et al., 1977).

Eq. (2) describes the forced convection sensible heat, while Eq. (3) describes free convection. Definitions for all parameters are given in Tables 1 and 2. Free convection is due to buoyancy of near-surface air, while the forced term is due to wind advection. The terms for mass loss through sublimation and associated latent heat removal are similar, as shown below. Sensible heat transfer could also exert a minor influence on the regional surface temperature as well. However, as described below, we use a simplistic model for atmospheric temperatures, controlled by the regional surface temperature, so we ignore this effect. It is more relevant for the ice surface, which may be at a significantly different temperature than the atmosphere.

An estimate of near-surface atmospheric temperature is needed for these equations. This temperature is that of the near-surface air for purposes of modeling heat transfer; it is not directly related to the downwelling atmospheric infrared flux. Williams et al. (2008) addressed a similar situation by setting the atmospheric tempera-

Table 2
List of model variables.

Parameter	Description	Units
b	Exponent for atmospheric temperature parameterization	Dimensionless
C_p	Atmospheric specific heat	$\text{J kg}^{-1} \text{ K}^{-1}$
D	Diffusion coefficient for H_2O in CO_2	$\text{m}^2 \text{ s}^{-1}$
e	Atmospheric water vapor partial pressure	Pa
e_{sat}	Saturated water vapor partial pressure	Pa
g_m	Mass transfer conductance	
k_{atm}	Atmospheric thermal conductivity	$\text{W m}^{-1} \text{ K}^{-1}$
L	Length scale for free convection	m
m_{sub}	Ice sublimation mass flux	$\text{kg m}^{-2} \text{ s}^{-1}$
P_{atm}	Atmospheric pressure	Pa
Q_c	Conductive energy flux	$\text{J m}^{-2} \text{ s}^{-1}$
Q_{LWF}	Atmospheric long-wavelength (thermal) energy flux	$\text{J m}^{-2} \text{ s}^{-1}$
Q_{solar}	Solar energy flux	$\text{J m}^{-2} \text{ s}^{-1}$
SH	Sensible heat flux	$\text{J m}^{-2} \text{ s}^{-1}$
T_{atm}	Near-surface atmospheric temperature	K
T_{bl}	Boundary layer temperature	K
T_{min}	Most recent diurnal minimum in T_{reg}	K
T_{reg}	Regional surface temperature	K
T_{surf}	Ice surface temperature	K
U	Energy for a model layer	J m^{-2}
u_{wind}	Wind speed	m s^{-1}
z_0	Surface roughness parameter	m
$\Delta \eta$	Difference between atmospheric and surface gas water mass fractions	Dimensionless
μ	Dynamic viscosity	Pa s
ν	Kinematic viscosity	$\text{m}^2 \text{ s}^{-1}$
$\Delta \rho / \rho$	Atmospheric and surface gas density difference, divided by a reference density	Dimensionless
ρ_{atm}	Atmospheric density	kg m^{-3}
ρ_{ave}	Average of ρ_{atm} and ρ_{surf}	kg m^{-3}
ρ_{surf}	Density of saturated surface gas	kg m^{-3}

ture to be the same as that of a sandy surface in a second thermal model. We use a similar approach, running a parallel thermal model with the parameters of the original ground surface. However, we note that the atmospheric temperature is not exactly the same as that of the regional surface, even very near the ground. Hess et al. (1976, 1977) found that in diurnal cycles at the Viking Lander sites, the minimum air and surface temperatures were comparable, but the maximum atmospheric temperature was roughly 20–25 K below the surface maximum. These measurements were made at a latitude and season similar to that of the ice exposures. We adopt the following parameterization for the near-surface atmospheric temperature:

$$T_{atm} = T_{min}^b T_{reg}^{1-b} \quad (4)$$

where T_{min} is the most recent diurnal minimum in the regional surface temperature and T_{reg} is the current regional surface temperature. This ensures that the minimum temperatures match, and that the maximum atmospheric temperature is less than that of the surface. This equation is an arbitrary parameterization, not based on any real atmospheric model. However, it has the advantage that a family of temperature models can be explored by varying the single parameter b , which effectively encapsulates variation in all of the parameters that could affect atmospheric temperature. It does not include the possibility that the temperature curves are phase-shifted in time, but air temperatures at the Viking sites peaked in early afternoon (Hess et al., 1977), as do surface temperatures. The shape of the curve could also be different, but appears similar in Fig. 6 of Hess et al. (1977), and so we consider this acceptable. For typical martian temperatures, we found that $b = 0.2$ roughly matches the ~20–25 K peak temperature difference observed at the Viking sites in summertime. However, the real martian atmosphere may have temperature variations over height ranges of decimeters (Schofield et al., 1997) and the relationship between atmospheric and surface temperature could vary. Therefore, we tested several values of b .

Our model can incorporate multiple material layers, and we experimented with two- and three-layer initial models. (The number of layers here refers to the number of material layers, not the number of model layers.) We can vary both the depth to ice and the ice layer thickness. At the time of impact, the upper soil layer is removed, exposing the ice. Although it is possible that impacts could excavate some amount of ice, the very high conductivity of ice means that this will have a small effect on the initial temperature profile. We thin the topmost model layer over time based on the calculated sublimation. The total sublimated thicknesses are often much less than one model layer over the relevant timescales, rendering this a minor effect.

For site 1, ice is exposed on crater floors, and so we incorporate shading due to the walls of the surrounding crater, which cuts off incident illumination. For simplicity, we assume that the ice still receives radiation from and emits to a completely open sky, without intervening crater walls. This approximation causes slightly cooler temperatures than would be expected, which will lead to an underestimate of sublimation; reradiated heat from the ground will typically be more than that from an equivalent solid angle of sky, since in our model for long-wavelength atmospheric radiation the flux from the sky is equivalent to an effective blackbody temperature much less than that of the ground. Moreover, this neglects reflected light from the crater walls.

2.2. Sublimation model

Like sensible heat, latent heat flux is described by free and forced-convection terms. We calculate the mass flux due to sublimation using

$$m_{forced} = M_w \frac{1}{kT} A u_{wind} (e_{sat} - e) \quad (5)$$

$$m_{free} = 0.14 \Delta \eta \rho_{ave} D \left(\left(\frac{\Delta \rho}{\rho} \right) \left(\frac{g}{\sqrt{2}} \right) \left(\frac{v}{D} \right) \right)^{\frac{1}{2}} \quad (6)$$

$$m_{sub} = m_{forced} + m_{free}$$

We use a sign convention such that both equations are positive if mass is lost from the surface. Eq. (6) is closely related to the free-convection equation derived by Ingersoll (1970) and a similar expression from Hecht (2002), while versions of Eq. (5) are derived by Paterson (1994) and Ivanov and Muhleman (2000). The mass is multiplied by the latent heat of sublimation to calculate the latent heat effect in Eq. (1). We also use these calculated values to track the total mass per unit area lost to sublimation as a function of time.

Following Toon et al. (1980) and Williams et al. (2008), we use the sum of the free and forced convection equations to calculate total sublimation. In heat transfer formalism, free and forced convection are coupled in ways more complex than simple addition (e.g. Incropera and de Witt, 1985), so caution is warranted in simply adding the two equations. However, Eq. (5) is derived differently from heat-transfer approaches to forced convection (e.g. Hecht, 2002), applying to a natural surface, and so does not simply fit the standard correlations. Adding the two equations gives a baseline zero-wind value and a linear increase in sublimation rate with wind speed, which is qualitatively consistent with the best-fit behavior reported under small-scale experimental conditions (Chittenden et al., 2008). Some more complex transitional behavior is likely at low wind speeds and may even be visible in the data of Chittenden et al., as there appears to be little increase in sublimation at low wind speeds. However, given the uncertainties in other parameters such as the drag coefficient and the translation from free convection over a discrete plate to a natural surface, we have opted for this simple approach. The general nature of our conclusions below would not be significantly altered even if we took an extreme approach and used only the larger of the free and forced sublimation values at each timestep.

The diffusion coefficient D and kinematic viscosity ν in Eq. (6) are calculated using the following equations from Chittenden et al. (2008) and references therein:

$$D = (1.387 \times 10^{-5}) \left(\frac{T_{bl}}{273.15} \right)^{\frac{3}{2}} \left(\frac{10^5}{P_{atm}} \right) \quad (7)$$

$$\nu = (1.48 \times 10^{-5}) \left(\frac{RT_{bl}}{m_c P_{atm}} \right) \left(\frac{240 + 293.15}{240 + T_{bl}} \right) \left(\frac{T_{bl}}{293.15} \right)^{\frac{3}{2}} \quad (8)$$

The relevant temperature for calculating these values is that of the boundary layer, T_{bl} , which can be set to the average of the ice and atmospheric temperatures (Hecht, 2002).

The term $\Delta \rho / \rho$ is the ratio of the density difference between saturated and background atmospheric gases to an atmospheric density. The atmospheric density is variously given as the density of near-surface gas, or as the average of near-surface and atmospheric density. Ingersoll (1970) provides the following expression for $\Delta \rho / \rho$ in an atmosphere at the same temperature as the surface, with no background water vapor content:

$$\frac{\Delta \rho}{\rho} = \frac{(m_c - m_w) e_{sat}}{m_c P_{atm} - (m_c - m_w) e_{sat}} \quad (9)$$

This expression has been consistently used by other workers in applying free-convection equations to estimate sublimation rates on Mars. However, this expression only applies at zero relative humidity and for an atmosphere and surface at the same temperature. The martian atmosphere may become saturated, particularly at night or in the winter, and in this case the assumed zero humidity is inappropriate. Incorporation of temperature effects can also have

a relevant effect on the buoyancy of saturated air. We employ a different form (following Mills (2001)), which accounts for the possibility that the background atmosphere has some humidity and that there may be temperature differences between the atmosphere near the surface and the background atmosphere, leading to thermal as well as compositional effects on buoyancy:

$$\frac{\Delta\rho}{\rho} = \frac{m_c \left(P_{atm} \left(\frac{T_{surf}}{T_{atm}} - 1 \right) \right) + (m_c - m_w) \left(e_{sat} - \frac{T_{surf}}{T_{atm}} e \right)}{\frac{1}{2} \left(m_c P_{atm} \left(\frac{T_{surf}}{T_{atm}} + 1 \right) - (m_c - m_w) \left(\frac{T_{surf}}{T_{atm}} e + e_{sat} \right) \right)} \quad (10)$$

If $\Delta\rho/\rho$ is less than zero (saturated surface air is not buoyant), we set it to zero; i.e., we assume forced convection provides a complete description of heat and mass transfer under those conditions. In general, this will occur when the atmosphere is much warmer than the ice surface, when some condensation might be expected.

We do not address the fate of vapor removed from the ice surface. During the day, the atmosphere has a low relative humidity and the sublimated vapor will be mixed into the atmosphere and transported away; the ice patches are far too small to have any effect on the overall atmospheric humidity far from the exposure. However, if the atmosphere is cold and saturated at night but the ice is relatively warm, the equations above imply that ice could still be removed by saturating near-surface gas warmed by the ice surface. Such vapor could recondense after traveling some short distance. If the condensed frost falls back to the ice or returns water vapor to the boundary layer above it before being transported away, this might suppress ice loss in this regime. This effect is potentially significant but poorly constrained. For instance, for a typical case at site 1, almost half of the modeled cumulative sublimation occurs in this regime. The sublimated vapor could snow out back onto the surface, but might form fog or be entrained and transported well away from the ice patch. We assume that all of the sublimated ice is removed.

The sublimation rate is strongly temperature-dependent, due to the nonlinear dependence of saturation pressure on temperature. It has recently been suggested that use of a saturation pressure set by the boundary layer temperature, rather than the ice temperature, gives a better match to experimental data (Chittenden et al., 2008). This approach was proposed to account for differences between experimentally measured sublimation rates and those calculated following Ingersoll (1970), similar to Eq. (6). Since the atmosphere may be warmer than the ice surface (although colder than the regional surface) at the warmest part of the day, this would significantly enhance modeled sublimation. However, convection parameterizations such as Eq. (6) are valid only over some range of the product GrSc, where Gr is the Grashof number and Sc is the Schmidt number, and most experiments appear to fall well outside the recommended range. For present purposes, we use Eq. (6) for free convection, and note that to the extent that this is incorrect, it is likely to underestimate sublimation (see Appendix A for further discussion). This formulation has the additional benefit that the convection rate does not depend on the length scale and so none need be assumed.

The drag coefficient A for forced convection is given by Paterson (1994) as:

$$A = k_0^2 / [\ln(z/z_0)]^2 \quad (11)$$

where z_0 is the surface roughness parameter, z is the height at which wind speed is measured and von Karman's constant k_0 is generally taken to be 0.4. Viking 2 measured wind speeds with a sensor at 1.6 m above the surface, finding typical values of 2–3 m/s (Hess et al., 1977). Surface roughness parameters range from 0.02 to 6 mm for various snow and ice surfaces on Earth, corresponding to coefficients from 0.0012 to 0.005 for the Viking sensor height. Paterson recommends a value of 0.002 for ice; we take this

as our nominal value, in the absence of any available measurements at the sites considered, but note that this value may be different for a surface freshly excavated by an impact. Variations in the drag coefficient are equivalent to variations in the wind speed since they are always multiplied, so we examined different wind speeds but did not vary the drag coefficient, following the approach of Williams et al. (2008). Such variations may also be taken to encompass other uncertainties associated with the forced-convection term, which nominally assumes an atmosphere with an adiabatic temperature gradient.

3. Model inputs

3.1. Model scenarios

Site 1 of Byrne et al. (2009) has the best-constrained history from HiRISE and CTX observations. (Table 3 gives basic information about each of the five sites from Byrne et al.) The site is at 46°N, 177°E, on lowlands east of the Phlegra Montes. Ice is exposed on the floors of two craters (Fig. 1) in a crater cluster that formed between L_s 81 and L_s 111. Polygonal terrain, which is likely due to repeated thermal contraction cracking, provides additional evidence for ground ice, although in principle the polygons could be relict landforms. The ice at site 1 was first observed by HiRISE at L_s 126 and has been observed to fade completely, disappearing between L_s 162 and L_s 180.

We consider a variety of scenarios for the impact at site 1. The primary variation in initial conditions is the ice thickness; it is likely that the thickness of ice or icy ground is at least close to the 5–10 m spacing of the thermal contraction cracks observed at the site. We have considered ice extending to the bottom of the model, as well as 5 m of ice underlain by dry soil; a thinner icy layer would raise the amplitude of temperature variations, enhancing sublimation. We assume an initial depth to the ice table of 0.51 m, the nominal value of Byrne et al. (2009), but modest variations in this depth have little effect on the initial temperature profile. In all cases we uncover the ice at the time of impact. In reality, some ice may be excavated by the impact event rather than simply uncovered, but ice temperature changes slowly with depth due to high thermal conductivity, and so this will cause only minor inaccuracy. We assume topographic shading appropriate for the floor of a flat crater with a depth/diameter ratio of 0.2, though the craters at site 1 are likely shallower than this (Byrne et al., 2009); the greater shading leads to a conservative estimate of sublimation.

We do not consider the effect of impact heating on the initial temperature structure. While the impact may significantly raise the temperature of the upper centimeters of the ice and perhaps even cause some melting (Reufer et al., 2009), this heat will largely be deposited within the diurnal thermal skin depth of ice. Hence, the thermal anomaly will be short-lived relative to the timescale over which ice is observed. We omit this effect and so underestimate the initial sublimation by some amount.

Table 3
Site properties.

	Lat. (°N) ^a	Lon. (°E)	Albedo	Thermal inertia (J m ⁻² K ⁻¹ s ^{-1/2})	Ice table depth ^b (m)
Site 1	46.3	176.9	0.24	233	0.51
Site 2	43.3	164.2	0.27	178	0.74
Site 3	55.6	150.6	0.15	265	0.12
Site 4	45.1	164.7	0.26	165	0.38
Site 5	46.2	188.5	0.25	187	0.14

^a Planetocentric.

^b From Mellon et al. (2004), as given by Byrne et al. (2009).

At sites 2–5, the ice exposures are on crater walls and ejecta, rather than on the floor (Fig. 2). This suggests excavation completely through the layer producing visible ice, and emplacement of ice on top of the local regolith. These sites present a large range of geometries: ice on crater ejecta is essentially a flat exposure, while that on crater walls may be on very steep slopes and influenced by complex reflection and reradiation and varying degrees of shading. Rather than attempt to account for these complex geometries in detail, we assume flat topography for sites 2–5, omitting the topographic shading discussed above. This is a fair approximation for the ice in crater ejecta, less so for the more complex cases where ice is exposed within or draped over a crater wall. We use calculated equilibrium ice table depths for each site (Mellon et al., 2004; Byrne et al., 2009), given in Table 3, to set the depth to ice for the initial models. For these sites we model sublimation from a 10-cm layer of ice emplaced on top of the original layered structure, as an approximation for icy ejecta emplaced on the surface.

As a more conservative estimate of the total sublimation at sites 2–5, we also examined scenarios where we exposed the ice table rather than emplacing ice on top of the regolith. For these scenarios we assumed no topographic shading, but did include estimated lateral heat conduction. The sublimation values from these cases are almost certainly underestimates, since regolith underlying ice will trap heat near the surface. Hence, these may be regarded as conservative estimates for these sites.

For these sites, the true nature of the exposures may be a mix of these two extremes. The geometries are in fact significantly more complex than emplacing or exposing a uniform layer of ice on otherwise flat terrain, and we have also omitted effects of possible regional slopes. The ice patches shrink significantly over time; at site 4, for instance, there is little ice on the ejecta and the exposure appears to be largely confined to the crater walls by L_s 185. Shrinking implies that either the ice thickness or the dust content of the ice is non-uniform, or that small-scale geometric effects play a role in sublimation rates and ice survival. It is very possible that all of these effects are significant. Moreover, ice exposures occurring in crater walls will receive insolation significantly different than flat terrain at the same location. Given the small scale of the craters, slope temperatures may also be influenced by lateral conduction from ground behind the slope, which will experience significant seasonal temperature variations to depths comparable to the crater depths. Hence, the geometry at each site will have complex effects on the temperatures, beyond the scope of our model.

3.2. Input parameters

We use thermal inertia values from the 20 pixel/degree (3 km/pixel at the equator) map of Putzig and Mellon (2007) to estimate the regolith thermal conductivity, using an assumed density of 1650 kg m^{-3} and heat capacity C_p of $837 \text{ J kg}^{-1} \text{ K}^{-1}$ (Mellon et al., 2004). As there is considerable scatter in thermal inertia values, we choose the median nighttime thermal inertia in a 5×5 pixel area centered on each impact site. Thermal conductivity of the martian regolith does depend on temperature (Zent et al., 2009) and vertical variations in material properties are possible, but poorly constrained. For simplicity, we assume a constant thermal conductivity for all regolith material at each site. We use ice thermophysical properties appropriate for 200 K (Aharonson and Schorghofer, 2006), neglecting the small variations due to temperature. As discussed below, it is likely that some of the ice in question is pore-filling ice. For simplicity, we use the thermophysical properties of pure ice, which has thermal inertia of $2137 \text{ J m}^{-2} \text{ K}^{-1} \text{ s}^{-1/2}$, compared with $2290 \text{ J m}^{-2} \text{ K}^{-1} \text{ s}^{-1/2}$ for ice-cemented ground using the parameters of Mellon et al. (2004). This is sufficiently similar as to have only a minor effect on the temperature distribu-

tion. For the regional models, we use measured Thermal Emission Spectrometer (TES) bolometric albedos (Christensen et al., 2001). The sites are typically bland in HiRISE color apart from the impact effects, so it is likely that the albedos are sufficiently uniform to apply the TES value at smaller scales. Table 3 shows the thermal inertia and regional albedo for each site.

We used initial albedos of 0.3–0.5 for exposed ice at site 1, consistent with clean or slightly dirty ice (Paterson, 1994). (Note that shock effects from the impact could affect the albedo, for instance by forming reflective fracture surfaces.) The ice patches at site 1 are brighter than the dark zones around the craters (Byrne et al., 2009), which may be representative of the soil at some depth. Relative to the adjacent plains, the patches are bright in the HiRISE blue–green filter but darker in red and near-IR, even at the time of the first HiRISE image of the site. Consequently, the initial albedos used may be too high (in particular, 0.5 is likely an extreme case), which will tend to underestimate sublimation. The ice is observed to fade over time. For site 1, we approximate this effect by forcing the ice albedo to darken linearly over time to a final value of 0.2 at L_s 171, the midpoint between the last HiRISE image showing ice and the first without any ice visible. This albedo is slightly darker than the plains surrounding site 1, consistent with the observed brightness ratios. Linear darkening roughly approximates the behavior observed by Byrne et al. (2009), but is simplistic since the true albedo will depend on the dust content of the ice and possible grain growth within it, the sublimation history, and atmospheric deposition or removal of dust.

Darkening is presumably due, at least in part, to development of an increasingly opaque lag or expansion of the area within each pixel covered by such a lag. Lateral heat conduction over scales of a few centimeters in ice is rapid, and so it is reasonable to approximate the albedo of the patch as fading even if sub-pixel patches remain bright. For site 1, all pixels of ice appear to fade together and the patch shrinks only minimally before disappearing, consistent with uniform accumulation of a lag or with very small-scale patchiness. Therefore, the approximation of a uniformly fading albedo is reasonable here.

At sites 2–5, the exposed ice brightness is higher than the undisturbed surroundings in all filters in the initial HiRISE images, by factors ranging from 1.1 to 4.2 depending on site and color band (Byrne et al., 2009). (The highest ratio for each band is found at site 3, likely because the region has a much lower albedo rather than because of any inherent difference in the ice.) The albedo history is more complex at these sites, as the ice patches both fade and shrink; pixels near the edge lose any sign of ice well before those at the core. There was also still ice extant at each of these sites at the time of the most recent HiRISE image. However, it does appear that the patches darken over time. Rather than attempt to model this level of complexity in detail, we assume initial albedos of 0.3, 0.4 and 0.5 and a final albedo of 0.3 reached at the time of the last HiRISE image. Byrne et al. (2009) give intervals in which the impacts could have occurred; we examined impact times at the end of the interval and at either the interval midpoint or L_s 60, whichever occurred later. The L_s 60 cutoff was imposed because some of the sites have possible impact times spanning over a year, but the observed timescales of fading suggests relatively recent events. If the impacts occurred earlier, more sublimation would be expected.

Atmospheric water vapor pressure (Smith, 2002) varies systematically with season and latitude, in addition to geographic variations. As the observed sublimation occurred during northern summer, we estimated the summertime near-surface partial pressure of water vapor using Eq. (C4) of Schorghofer and Aharonson (2005), with column abundances and condensation heights estimated from Smith (2002). This may be an overestimate; recent work has suggested that TES data systematically overestimated

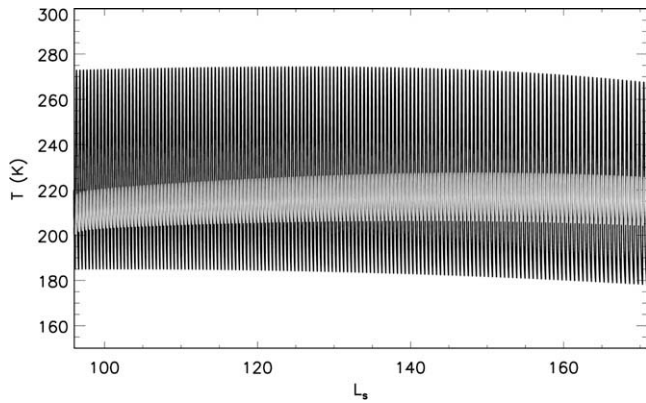


Fig. 4. Model ice temperatures (gray) as well as regional surface temperatures (black) over the interval during which ice was exposed at site 1, for baseline case assuming that the impact occurred at L_s 96 and ice disappeared at L_s 171.

water vapor abundance (Fouchet et al., 2007), and summertime water vapor content is higher than at other seasons. Using a high value will suppress sublimation at some times of year, giving a lower bound on sublimation. If the atmospheric temperature falls below the frost point at night, we hold the vapor pressure at saturation (similar to Mellon and Jakosky (1993)). This behavior is qualitatively consistent with that observed by the Phoenix Lander (Hudson et al., 2009), although the atmospheric vapor pressure was reported to drop before the atmosphere reaches the frost point. This may be due to regolith adsorption or the effect of perchlorate salts. All else being equal, earlier reduction in the vapor content would slightly increase sublimation. We do not specifically track the state of water vapor temporarily removed from the regional atmosphere due to saturation. Mid-latitude atmospheric water vapor content is equivalent to at most tens of precipitable microns, and nighttime saturation may lead to fogs or clouds or adsorption into the regolith rather than formation of surface frost (Schorghofer and Edgett, 2006). Additionally, the ice patches will be warmer

than the surrounding ground at night (Fig. 4) due to a high thermal inertia, inhibiting condensation there.

Typical summer wind speeds measured at the Viking 2 landing site at a similar latitude on the northern plains were 2–3 m/s (Hess et al., 1977). Winds at the Phoenix landing site ranged from 1 to 12 m/s, but were most commonly 2–6 m/s (Holstein-Rathlou et al., 2009). We used a nominal value of 2.5 m/s, and considered extremes of 0 and 7.5 m/s. Although zero wind is unlikely, ice on crater floors may be sheltered from the wind, so this is an extreme but potentially relevant case. We note that the forced-convection sublimation rate is linear with wind speed (Eq. (4)), and so using an averaged rather than time-varying value does not introduce any error unless wind speed also correlates with time of day (and thus the saturated vapor pressure, which does not vary linearly with temperature). The winds at the Viking 2 site reported by Hess et al. did show some systematic diurnal variation, but in the absence of any data for the crater sites we have simply assumed constant speed.

4. Results

For each site, we simulated a variety of scenarios exploring all combinations of the parameters given in Table 4. Table 5 summarizes the range of results for all five sites. Sublimation mass fluxes from each timestep are converted to sublimated thicknesses of ice. For each site, the “baseline” case assumes an initial ice albedo of 0.4, ice extending to depth, 2.5 m/s wind and $b = 0.2$. The impact time is the midpoint value for site 1, and the later impact time for sites 2–5 where only two impact times were considered. This baseline represents a reasonable intermediate value in parameter space, but not a definitive best estimate of the site properties.

Fig. 4 shows the temperature history of an ice patch at site 1 with intermediate parameters, in comparison with the regional surface temperatures over the same time interval. For site 1, the modeled cumulative sublimation at L_s 171 was generally between 0.35 and 4 mm, with a few extreme cases above 6 mm. Fig. 5 shows

Table 4
Parameters varied in thermal model.

Parameter	Values considered				
	Site 1	Site 2	Site 3	Site 4	Site 5
Impact L_s	81, 96, 111	60, 94	76, 129	74, 127	60, 92
Final L_s^a	171	235	190	222	204
Ice table thickness (m)	5, ∞	5, ∞	5, ∞	5, ∞	5, ∞
Initial ice albedo	0.3, 0.4, 0.5	0.3, 0.4, 0.5	0.3, 0.4, 0.5	0.3, 0.4, 0.5	0.3, 0.4, 0.5
Final ice albedo	0.2	0.3	0.3	0.3	0.3
Wind speed (m/s)	0.0, 2.5, 7.5	0.0, 2.5, 7.5	0.0, 2.5, 7.5	0.0, 2.5, 7.5	0.0, 2.5, 7.5
Atmospheric exponent b^b	0.1, 0.2, 0.3	0.1, 0.2, 0.3	0.1, 0.2, 0.3	0.1, 0.2, 0.3	0.1, 0.2, 0.3

^a Midpoint time between last image with ice and first image without ice for site 1, last HiRISE image (showing ice) for sites 2–5. A HiRISE image of site 5 at L_s 259 suggests that ice was still present at that time, but the image is hazy, so we have conservatively used the earlier date. Image ESP_014264_2235 shows ice still extant at site 2 at L_s 320, but winter sublimation is expected to be negligible.

^b See Eq. (4).

Table 5
Range of model results.

	Total sublimation at final time (mm)				
	Site 1	Site 2 ^a	Site 3 ^a	Site 4 ^a	Site 5 ^a
Minimum, all cases	0.35	2.1 (0.8)	0.23 (0.23)	0.89 (0.4)	1.9 (0.85)
Baseline	1.8	9.8 (2.6)	1.3 (0.88)	4.0 (1.2)	8.0 (2.6)
Maximum, all cases	6.9	57 (11.5)	20 (9.7)	44 (8.7)	42 (10.7)
Minimum, wind speed ≥ 2.5 m/s	0.97	4.1 (1.7)	0.58 (0.54)	1.7 (0.76)	3.8 (1.8)

Note: Decimal places given do not indicate any assessment of model accuracy. Sources of error are discussed in the text.

^a For sites 2–5, the initial value is that for the cases where a layer of ice is emplaced on top of regolith, and the value in parentheses is that for the cases where the ice table is exposed.

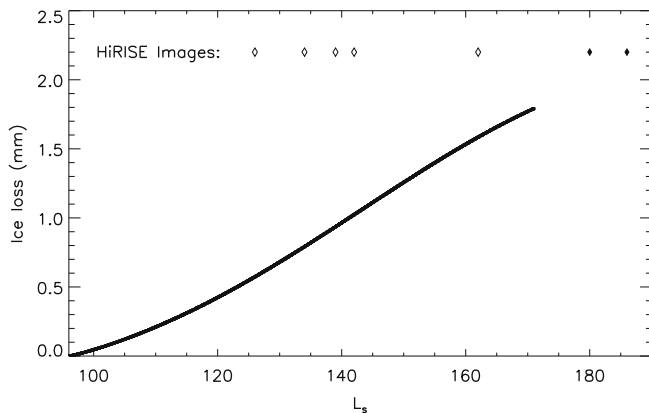


Fig. 5. Modeled cumulative sublimation history from the ice patch at site 1 for ice extending to depth, with intermediate values of other parameters. In this example, the impact occurred and sublimation commenced at L_s 96 and almost 2 mm of ice sublimated before the patch faded sometime between L_s 162 and 180; the line terminates at L_s 171, the midpoint time. Ice is likely still present and slowly sublimating through a lag after fading. Open diamonds indicate times of HiRISE images showing ice still present, while filled diamonds indicate times of images showing no visible ice.

a modeled sublimation history at site 1 for the baseline case described above, which gave 1.8 mm of sublimation. The lowest values were for those cases that assumed an initial albedo of 0.5 and zero wind. The minimum total sublimation in any case tested was 0.35 mm. Total sublimation before disappearance for each case would be somewhat less if the lag became opaque before L_s 171, but ice was visible until at least L_s 162; in the baseline case, 1.6 mm of sublimation occurred by that time.

The parameter with the strongest effect at site 1 is the wind speed. For otherwise equivalent cases, an increase from 0 to 7.5 m/s wind speed increases the total sublimation by a factor of 5–7, indicating the importance of forced convection. For cases with 2.5 or 7.5 m/s wind speed, total sublimation is always greater than 0.9 mm. Different values for ice albedo and impact time can also cause significant variation. For instance, cases with impact at L_s 81 had sublimated thicknesses about 1.8 times those with impact at L_s 111. (Note that since the albedo is assumed to darken linearly over the interval between impact and L_s 171, cases with later impacts darken more quickly over time.) The difference between a 5-m-thick ice layer and one extending to the bottom of the model was minor, as was the effect of the atmospheric temperature parameter.

Sites 2–5 show similar trends. Sublimated thicknesses are higher for cases where ice is emplaced on top of regolith, with baseline values of several millimeters and extremes of several centimeters. Site 3 experiences distinctly less sublimation than the other sites for comparable parameters due to its significantly higher latitude. For these sites, the ice exposures are not sheltered from the wind, and so the cases with zero wind speed are particularly unlikely. Everywhere except site 3, the minimum sublimated thickness for non-zero wind cases is over a millimeter. For these sites, the cases where ice was exposed generally give values similar to site 1; these may be reasonable approximations for parts of the geometrically complex exposures.

5. Discussion

5.1. Model uncertainties and interpretation

We have made mostly conservative assumptions with respect to calculating the total sublimation from the ice, or tested a range of values encompassing most plausible cases. We use a constant

rather than diurnally varying value for Q_{LWF} , which tends to reduce the amplitude of the diurnal temperature fluctuation. We ignore heating from the impact, which could significantly enhance sublimation for a brief interval after the impact event. The corrections made for topography at site 1 are conservative: the crater depth/diameter ratio assumed is high, leading to excess shading, and we ignore reflection and radiation from crater walls, instead retaining absorption from and emission to a cold sky. We assume a constant and relatively high daytime atmospheric water vapor content. Our free-convection parameterization cuts off sublimation by this process if the atmosphere becomes significantly warmer than the surface during the warmest part of the day, and should under-predict sublimation for some possible conditions (Appendix A). The most significant potentially non-conservative assumption is the removal of sublimated ice when the surface is warmer than a saturated atmosphere. Also, our lateral heat flow estimate is simplistic and could be an underestimate. While some aspects of the model are poorly constrained, model error for site 1 is most likely to be in the direction of under-predicting sublimation. Therefore, it appears probable that impact-exposed ice remained visible over a period in which over a millimeter of net ice ablation occurred.

For sites 2–5, most of these conservative factors apply, but we omit heat losses to lateral conduction for the cases where ice is emplaced on top of the regolith, as discussed above. Such cases are more sensitive to errors in the depth to the ice table and to the assumed thickness of the deposited ice layer; a thinner ice layer would be prone to greater temperature fluctuations and sublimate even more rapidly, while the depth to the ice table controls the thickness of the insulating underlying regolith. However, the cases where we exposed ice at these sites (similar to the scenario for site 1, but without any shading) resulted in sublimated thicknesses which are comparable to or larger than those calculated for site 1, i.e. baseline values of about a millimeter or more. These are not realistic scenarios, but give conservative estimates that still indicate at least one to several millimeters of sublimation.

Interpretation of the model results for sites 2–5 is complicated by the geometries of the exposures, which shrink over time and have complex interactions with topography. We have assumed level exposures for each site. All else being equal, ice should sublimate faster than modeled on equator-facing slopes (south-facing for all of these sites) and slower if facing the pole. Sites 3 and 5 are comparatively straightforward, as both have ice still extant on relatively flat ejecta at the end times given in Table 4, but the exposures did shrink somewhat over time. At site 2, ice faded from a north-facing slope within the crater, and the last remnant of visible ice appears to be that at the crater rim and possibly even on south-facing ejecta. The interpretation of the model results for site 4 is perhaps the most uncertain, since ice disappears from the crater ejecta by L_s 185 but remains on north- and south-facing crater walls at L_s 222, the end of the model runs and the time of the most recent HiRISE image. Given this, the cases with ice emplaced on top of the regolith are probably not appropriate by the endpoint of the model run. The slopes within the craters are significant and should have a large effect on the incident insolation and thus sublimation. Sublimation on pole-facing slopes at each site should be less than the model indicates. A further slope-induced complication is the possibility of lag particles falling downslope. However, ice was still visible at the time of the most recent HiRISE image of each of these four sites, so the sublimation to date has not been enough to produce an opaque lag over all of the ice surface.

We do not account for the effects of lag formation on sublimation rates, but those are unlikely to become very important before the lag is opaque. It is likely that most of the soil at the impact sites is silt-sized grains or smaller, as was observed at the Viking 2 landing site (Moore et al., 1977, 1987). For fine-grained material, coatings as thin as 40 μm (0.04 mm) may be optically thick at HiRISE

red wavelengths, and perhaps as little as 17 μm in the blue–green band (Fischer and Pieters, 1993). Depending on wavelength and the covering layer density, values up to 400 μm (0.4 mm) may be required for complete opacity (Morris et al., 2001). Experimentally, sublimation rates through lags of order a centimeter thick are close to those predicted by Ingersoll's (1970) free-convection equation (Hudson et al., 2007). Although this comparison is subject to the issue of experimental scale noted in Section 2.2, sublimation of bare ice at similar scales gives fluxes only slightly higher than that predicted from Ingersoll (e.g. Chittenden et al., 2008). Calculation confirms that this is reasonable; for typical Mars surface conditions, the rate of sublimation loss through a lag (calculated following Hudson et al.) is greater than the convective sublimation loss rate until the lag thickness is greater than a few centimeters. This indicates that convective removal of water vapor, not diffusion through a lag, is the rate-limiting process while the lag is thin.

5.2. Dust content of exposed ice

Are the model results in Table 5 compatible with the ice exposures being pore ice? This would be a reasonable interpretation if the sublimated thicknesses were comparable to the thickness of an opaque dust lag. For an intermediate opaque-lag thickness of 0.1 mm, the baseline cases yield dust content estimates of 1–10 vol.%, assuming that the surface is uniform at the sub-pixel scale and that the lag accumulates entirely from dust within the ice. If the highest value noted above (0.4 mm) is applied, our lowest calculated sublimated thicknesses for sites 1 and 3 would be roughly compatible with pore ice. The minimum result from site 4 for cases where the ice table was exposed also falls in this range; this model may be a better fit for ice in the crater walls than that where ice is emplaced in the ejecta.

However, we consider pore ice unlikely for several reasons. Those model cases that produce less than half a millimeter of sublimation at site 1 are extremes: they assume no wind, so that only free convection operates. While the crater rim may provide shelter at site 1, this clearly is an extreme assumption, and much of the ice at sites 2–5 does not have any significant protection from the wind. For sites 2 and 5, none of the cases with non-zero wind gave less than a millimeter of total sublimation. The low-sublimation cases also require high initial albedos; at site 1, no case with an initial albedo of 0.3 produced less than half a millimeter of sublimation. This is the lowest albedo we considered, but it may be appropriate for site 1 since the ice exposure was actually darker than the surrounding plains (although brighter than the dark blast zones) in the red and near-IR channels during the entire period of HiRISE observations, fading to nearly match the blast-zone albedo (Byrne et al., 2009). The ice patches are brightest and most distinct in the HiRISE blue–green filter, even though the thickness of an optically thick layer is a factor of several smaller at short wavelengths compared with red and near-IR. Furthermore, ice remained visible at sites 2–5 at the times of the most recent HiRISE images, indicating that the thicknesses sublimated at those times are insufficient to produce an opaque lag. These factors combined with the generally conservative model assumptions strongly suggest that the observed ice contains less soil than pore-filling ground ice.

At the Phoenix landing site, both pore-filling ice and nearly pure ice were observed. Parts of the relatively pure ice in the “Dodo-Goldilocks” trench remained distinctly bright for several months, fading as a lag slowly accumulated over an L_s range similar to that during which the impact exposures were observed to fade (Blaney et al., 2009). This behavior and timescale is very similar to that of the impact-exposed ice at lower latitudes. Ice-cemented ground at the Phoenix site matched the appearance of dry soil within five sols (Smith et al., 2009). All else being equal, sublimation rates and lag formation are likely to be faster at lower latitude, and Phoenix

landed more than 20° north of most of the impact ice exposures. Smith et al. (2009, supplementary online material) suggest 3 mm of sublimation over 42 sols in the “Dodo-Goldilocks” trench, which also suggests that our calculated sublimated thicknesses are conservative, as intended.

It is also possible to test the pore-filling ice model more directly. We examined a scenario for site 1 where the exposed substrate had a constant albedo matching the surrounding terrain, with pore-filling ice extending to depth and intermediate values for other parameters from Table 4. This is intended as a proxy for exposure of ice-cemented soil, although at the Phoenix landing site pore-ice exposures appeared darker than soil alone from some angles due to scattering within the ice (Smith et al., 2009), and the surface albedo at the impact sites may be brighter than the inherent albedo of the regolith material a few centimeters below the surface due to a cover of atmospherically deposited dust. For this run we used thermo-physical properties of ice-cemented soil. In this case, the total sublimation at L_s 171 was 2.6 mm; between impact at L_s 96 and the time of the first HiRISE image at L_s 126, there was over a millimeter of sublimation, enough to produce an opaque lag for pore-filling ice. (Note that the conservative factors given above also apply to this scenario.) Only a very high initial albedo could slow the sublimation rate sufficiently to make this case consistent with even the most generous assumptions about opacity.

A high albedo is not likely for exposed ice-cemented ground unless impact processes such as formation of fractures brighten the ground ice significantly. Experimental impacts in silicate–ice mixtures at very small scales have been observed to result in some brightening (Koschny and Grün, 2001). However, following Clark et al. (1983), the timescale for ice grain growth from infinitesimal size to 5 μm at 215 K is roughly four days. (Kieffer (1990) suggests even higher growth rates.) Even if the impact initially pulverized the ice, few-micron grains would grow rapidly. For few-micron-diameter dust particles typical of much martian soil (Moore et al., 1987), this ice grain size is not consistent with a high albedo unless the dust content is on the order of 10% by mass or less (Kieffer, 1990). Several caveats apply; trapping of bubbles in annealed fractures could affect the albedo, larger particle sizes would allow much higher dust contents and grain growth may be complicated if confined to narrow pore spaces. However, the bulk ice grain size could be significantly higher than 5 μm , in which case a high albedo would require larger dust particles or a smaller dust fraction.

A more direct argument against brightening of pore ice is the morphology of the other largest craters at site 1, which are of comparable size but do not show visible ice. Several of these are flat-floored, consistent with the existence of a resistant layer (Melosh, 1989) such as ice or ice-cemented ground. The largest crater at site 1 (Fig. 6) falls into this category. It is likely that these excavated to ice-cemented ground, which no longer shows any visible difference from soil; the calculation above, as well as Phoenix observations, show that it is more than reasonable for interstitial ice to develop an opaque lag by the time of the first HiRISE image. Since these craters appear morphologically compatible with exposure of pore-filling ice, this suggests that impact effects do not cause pore ice to brighten enough that it could remain visibly exposed for months. Similarly, we note that the floor of the crater at site 3 is in fact distinctly dark, while the icy ejecta is very bright. If impact-induced brightening had a major effect on pore ice albedo, it is likely that the crater floors would all be brightened. It is likely that some other factor, most likely ice purity, causes the continuing visibility of ice.

Removal of dust by the wind could prevent formation of a sublimation lag and give the appearance of relatively clean ice. However, the opposite effect appears more likely. Some amount of lag development at site 1 may be due to deposition of airfall dust, since the dark blast zones around the craters appear to fade over time



Fig. 6. Largest crater in cluster at site 1 (red band of HiRISE image PSP_009978_2265). Unlike the craters at the same site in Fig. 1, this crater does not visibly expose ice, although they formed simultaneously; this crater is over half a meter deep. The flat floor may be caused by a strength change due to excavation to interstitial ice, which would rapidly develop an opaque lag.

(Byrne et al., 2009). This reduces the implied soil content within the sublimated thickness by some unknown amount.

Impacts could melt or vaporize some amount of ice (Reufer et al., 2009), and it is possible that the ice we observe has been through phase changes and does not represent the original state of the ice table. However, some morphological evidence suggests that the ice purity is due to the conditions in the original ice. Melting of pore ice would probably form mud; if the meltwater remains liquid long enough to collect and pool, the liquid on crater walls and ejecta would have time to drain and we would not observe ice deposits there. Condensation of vaporized ice is also possible, but we observe flat-floored craters which probably excavated to the ice table but do not have associated ice exposures (Fig. 6). There is also no obvious reason why vapor deposition would be tightly concentrated on crater floors at some sites (site 1) and in ejecta at others (site 3). Crater floors and ejecta will be the warmest local surfaces immediately after impact, suppressing condensation. While some amount of impact modification has probably occurred, it is likely that much of the ice we observe is excavated solid material.

The simplest alternative to pore-filling ice is exposure of a uniform dust-poor icy layer, which sublimates until an opaque lag has accumulated. Subsequent sublimation will have little visible effect apart from very slow collapse of the crater. Taken at face value, volumetric dust contents of a few percent (up to at most around 30%) are implied by the relative thicknesses of an opaque lag and the baseline sublimation estimate for each location, depending on the thickness considered opaque. Ideally, it would be possible to find dust contents that matched the albedo and produced the right amount of dust to make an opaque lag after sublimation equal to the calculated thicknesses. In principle, the reflectance of ice–soil mixtures can be calculated, based on the dust content and the grain sizes of ice and dust (e.g. Clark, 1982). However, several factors make it difficult to do so accurately. The exposure could be a combination of dark soil and relatively bright ice, mixed at the sub-pixel level. Moreover, we lack strong constraints on the grain sizes of ice or dust or on the bubble content of the ice. Impact effects such as fracturing, melting or annealing from impact heat could alter these parameters in some thickness of ice, further complicating such an estimate.

5.3. Implications for ground ice on Mars

Sites 1, 2 and 4 are located on or near lobate aprons that resemble features recently shown to be debris-covered glaciers, and sim-

ilar aprons in the region appear to be largely ice (Safaenili et al., 2009). If this is also true at these impact sites, it is possible that the exposed material is the top of massive glacial ice. However, the morphologies in this region are complex and gradational, and the craters may not sit on true debris-covered glaciers. Even if the craters overlie glacial ice, it is possible that the debris overburden has a significant thickness and contains a complex ice table structure related to subsequent processes. The ice exposures at sites 2 and 4 are concentrated on crater walls and ejecta. At neither site does the deepest part of the crater appear particularly ice-rich, as might be expected for a simple scenario with a thin debris layer over extensive pure ice, although this could be affected by wall slumping. Sites 3 and 5 occur on plains without obvious geomorphic evidence for possible extant glaciers.

GRS measurements suggest high volumetric ice contents over broad areas polewards of $\sim 60^\circ$ lat. (e.g. Boynton et al., 2002; Feldman et al., 2007). These ice contents are larger than the pore space in typical soils, indicating excess ice. Our results suggest that potentially similar excess ice extends to lower latitudes. Mellon et al. (2008) argued that such high ice contents are at odds with the geomorphology of thermal contraction cracks at the Phoenix landing site at 68°N , as the observed polygon dimensions indicate that they formed in ice-cemented soil. As GRS is only sensitive to the upper decimeters of soil, they suggested that a layer with excess ice occurs near the top of an ice table that is otherwise close to pore-filling. Mellon et al. considered a number of possible scenarios for the production of high volumetric ice contents, including extremely porous soils, ice lens formation by migration of thin liquid films, or deposition of dusty snow. They noted that rocks and craters on the surface make a sublimation lag above recent snow unlikely. Some of the ice observed at the Phoenix site had a dust content of only a few percent (Smith et al., 2009), making extreme initial porosity unlikely to be the sole explanation for that deposit. On Earth, ice lens formation typically occurs when wet soil freezes and water migrates to a lens via thin films (e.g. Rempel, 2007). This scenario is unlikely to be common in recent martian history (Miller and Black, 2003), but Mellon et al. proposed that such a process could occur without bulk melting.

An additional possible mechanism was suggested by Fisher (2005). Cracking and differential contraction during cooling could open small spaces for vapor deposition of additional ice, leading to relatively high volumetric ice content after many cycles. This mechanism has some intriguing features. The surface material (which includes meter-scale boulders at some sites) need not be a lag from sublimation of dusty snow and liquid water is not required even in the form of thin films. It is interesting to note that one of the ice exposures at site 1 appears to be in line with a polygon crack (Fig. 1), since Fisher notes the possibility of forming ice wedges by cold-trapping water vapor in thermal contraction cracks. However, at least one other crater of comparable size at site 1 does appear to intersect a crack but lacks visible ice, so this may be coincidental. One significant uncertainty is the age of the ice; the ice observed at some of these sites may be unstable in the present climate (Byrne et al., 2009), while Fisher (2005) suggests timescales of 1–10 Ma for formation of very pure ice by this process, even at depths less than a meter. Ground ice could have been stable as recently as 10 ka ago due to variation in the argument of perihelion, but has likely been unstable and undergoing net loss during a significant fraction of recent history (e.g. Chamberlain and Boynton, 2007).

The geomorphic features observed at the sites of impact-exposed ice are consistent with the ice table structure suggested by Mellon et al. (2008). Among the five impact sites, we observe ice on crater floors, walls and ejecta. Ice on crater floors is consistent with craters excavating into, but not through, the relatively clean

upper part of the ice table. The observation of ice in the ejecta but not the crater floor at site 3 suggests that the lowest excavated material had relatively low ice content, while portions of the ejecta formed from a relatively pure ice layer. The layer must have a non-trivial thickness in order to be well-exposed by craters at each of the five northernmost new crater clusters imaged by HiRISE and to constitute a large fraction of the exposed ejecta at several sites. At site 1, ice is observed in two craters but absent in several others of comparable size and identical age, indicating inhomogeneities in either the ice table depth or the soil content of ice. The number of examples presently available is not sufficient to make generalizations about morphologic progression with crater size, particularly given probable variations in ice table structure with latitude, but the observed morphologies appear consistent with a shallow layer of very high ice content that is penetrated by some impacts and partially excavated by others. The underlying layer may be ice-cemented soil. Such ice would recede from view and appear as bare soil well before HiRISE observations could be made. Some caution is required in this morphological interpretation due to the possibility of ejecta fallback or wall slumping onto the crater floor.

Sublimation of ice from a relatively pure layer could have an effect on degradation of small mid- and high-latitude craters. Exposure of ice by the impact would lead to loss of material from parts of the crater walls through sublimation on a timescale of tens to hundreds of years, potentially leading to slumping of wall material. The magnitude of this effect would depend on the amount of relatively pure ice and its position within the crater; for ice layer thicknesses comparable to crater dimensions, significant degradation may be possible. This process could be a factor in the reported young crater retention age at high martian latitudes (Kreslavsky, 2009). It is possible that a similar process could affect ice-cemented soil to a lesser extent, since interstitial ice could initially support steeper slopes than loose soil. This process would be more effective on equator-facing slopes and might produce an observable asymmetry in crater profiles, depending on the amount of ice present and the significance of other modification processes.

Evidence for relatively pure ice in the mid-latitudes supports thermokarstic models for the origin of certain mid-latitude features such as scalloped depressions in Utopia Planitia. Formation of substantial depressions by thermokarst is puzzling if the only ice is pore ice deposited within a self-supporting regolith skeleton. Various authors have proposed a variety of processes to explain excess ice or produce depressions without it (e.g. Morgenstern et al., 2007; Lefort et al., 2009). Evidence for such ice in the mid-latitudes, regardless of the origin, supports the possibility of thermokarst and reduces the need to invoke other mechanisms for mass removal.

Future HiRISE and CTX observations of new impact ice exposures should lead to improved constraints on the nature of the martian ice table. A larger sampling will give more information about geographic variations in the occurrence of ice. In addition, if there are geographic variations in the thickness of excess ice, this may result in systematic differences in the appearance of the craters. Many more examples would be required to decouple geographic variations from those due to crater properties, but with ever-increasing repeat coverage area from CTX further detections are likely.

HiRISE observes ice exposed by recent impacts in the martian mid-latitudes. We find that modeled sublimation rates, in conjunction with the observed lifetime of ice, suggest that some of the ice exposed by these impacts has a low dust content; some process is required to produce excess ice in the shallow martian subsurface. This ice may comprise a layer above ice-cemented regolith. This supports existing models of the martian ice table structure, and suggests that this structure extends to the mid-latitudes.

Acknowledgments

We thank the Context Camera team for their rapid identification of potential fresh craters and cooperation in coordinating with HiRISE imaging, and the HiRISE operations staff for their work in obtaining the excellent images used in this work. Andrea Philippoff provided helpful comments on an early draft of this paper, and two anonymous referees provided detailed and useful reviews. This work was funded by the Mars Reconnaissance Orbiter project.

Appendix A. Free-convection equations

Standard equations for sublimation by free convection are based on an analogy with heat transfer and parameterizations of the transfer rate under various conditions. For sublimation, the typical parameterization used is that of a hot plate under cold fluid, equivalent to a saturated (buoyant) near-surface vapor under an undersaturated gas for mass transport purposes. Ingersoll (1970) gives the following equation for free-convection mass flux:

$$m = 0.17 \Delta \eta \rho_{surf} D \left(\left(\frac{\Delta \rho}{\rho} \right) \left(\frac{g}{v^2} \right) \right)^{\frac{1}{3}} \quad (A1)$$

This expression has been used frequently in studies of sublimation on Mars (see Table 1 for definitions of all parameters).

A similar expression may be derived following Mills (2001). Mills gives

$$Sh = 0.14 (GrSc)^{\frac{1}{3}}, \quad 2 \times 10^7 < GrSc < 3 \times 10^{10} \quad (A2)$$

where Gr is the Grashof number

$$Gr = \frac{gL^3(\Delta\rho/\rho)}{v^2} \quad (A3)$$

Sc is the Schmidt number

$$Sc = \frac{v}{D} \quad (A4)$$

and Sh is the Sherwood number.

Then the mass transfer conductance g_m is given by

$$g_m = \frac{\rho D}{L} Sh \quad (A5)$$

and the mass flux per unit area is

$$m = g_m \Delta \eta \quad (A6)$$

The mass flux of water vapor is thus

$$m = 0.14 \Delta \eta \rho_{ave} D \left(\left(\frac{\Delta \rho}{\rho} \right) \left(\frac{g}{v^2} \right) \left(\frac{v}{D} \right) \right)^{\frac{1}{3}} \quad (A7)$$

Hecht (2002) derives a similar equation for a similar range of GrSc, but with a leading coefficient of 0.15 instead of 0.14 due to a slightly different parameterization. Eq. (A1) is similar to Eq. (A7); however, for typical martian parameters, v/D is close to 0.5, and so A1 predicts moderately more sublimation than Eq. (A7) under many conditions. (This offset was also noted by Taylor et al. (2006).) Ingersoll (1970) gives several reasons why free-convection sublimation may be higher than expected, but we use Eq. (A7) as a conservative estimate.

Although Eq. (A7) is not dependent on length scale, the range of applicability in Eq. (A2) does depend strongly on L , via the Grashof number. The length scale relevant for an ice patch on the martian surface is not clear. The patch has a defined edge, but the atmosphere around the ice is also likely to convect since the ground surface is warmer than the atmosphere, although the density contrast will differ. There is not a distinct plate driving all of the convection in the system. For reasonable martian conditions, a length scale of

1 m gives $\text{GrSc} \sim 10^5\text{--}10^6$ for most $\Delta\rho/\rho$ greater than zero, while 5 m generally gives $\text{GrSc} > 10^7$. Note that if the relevant scale is that of the ice patch, the length scale is not the same as the width; it may be approximated as area/perimeter (Incropera and de Witt, 1985), or half the radius for a circular patch.

Martian conditions may be in a regime where $\text{GrSc} < 2 \times 10^7$. Mills (2001) gives

$$\text{Sh} = 0.54(\text{GrSc})^{\frac{1}{4}}, \quad 10^5 < \text{GrSc} < 2 \times 10^7 \quad (\text{A8})$$

The ratio of Eqs. (A2) and (A8) (and the mass fluxes derived from them) is

$$m_{\text{high}}/m_{\text{low}} = 0.26(\text{GrSc})^{\frac{1}{12}} \quad (\text{A9})$$

which is close to (but less than) 1 for GrSc as low as 10^5 . Hence if Eq. (A7) is applied outside the relevant range, it is not badly in error, and underestimates sublimation for the most extreme deviations. This is also consistent with experimental data at few-centimeter length scales (and thus small values of GrSc , on the order of 1–100), which in many cases find that Eq. (A1) may under-predict sublimation by factors of 2–4 (e.g. Taylor et al., 2006; Chittenden et al., 2008); it is likely that the small scales place the experiments in a regime where the theory does not apply accurately. This may account for part of the difference noted by Chittenden et al. (2008).

We therefore consider it likely Eq. (A7) gives a conservative estimate of ice loss. A broader question, not addressed here, is whether the parameterization for a finite plate translates well to an extensive natural surface.

Appendix B. Supplementary material

Supplementary data associated with this article can be found, in the online version, at doi:10.1016/j.icarus.2009.09.007.

References

- Aharonson, O., Schorghofer, N., 2006. Subsurface ice on Mars with rough topography. *J. Geophys. Res.* 111, E11007. doi:10.1029/2005JE002636.
- Blaney, D.L., and 13 colleagues, 2009. Multi-spectral imaging of the Phoenix landing site: Characteristics of surface and subsurface ice, rocks, and soils. *Lunar Planet. Sci. XL* (Abstract 2047).
- Boynton, W.V., and 24 colleagues, 2002. Distribution of hydrogen in the near surface of Mars: Evidence for subsurface ice deposits. *Science* 297, 81–85.
- Byrne, S., and 17 colleagues, 2009. Distribution of mid-latitude ground ice on Mars from new impact craters. *Science* 325, 1674–1676.
- Carr, M.H., 1990. D/H on Mars: Effects of floods, volcanism, impacts and polar processes. *Icarus* 87, 210–227.
- Chamberlain, M.A., Boynton, W.V., 2007. Response of martian ground ice to orbit-induced climate change. *J. Geophys. Res.* 112, E06009. doi:10.1029/2006JE002801.
- Chittenden, J.D., Chevrier, V., Roe, L.A., Bryson, K., Pilgrim, R., Sears, D.W.G., 2008. Experimental study of the effects of wind on the stability of water ice on Mars. *Icarus* 196, 477–487.
- Christensen, P.R., and 25 colleagues, 2001. Mars Global Surveyor Thermal Emission Spectrometer experiment: Investigation description and surface science results. *J. Geophys. Res.* 106 (E10), 23823–23871.
- Clark, R.N., 1982. Implications of using broadband photometry for compositional remote sensing of icy objects. *Icarus* 49, 244–257.
- Clark, R.N., Fanale, F.P., Zent, A.P., 1983. Frost grain metamorphism: Implications for remote sensing of planetary surfaces. *Icarus* 56, 233–245.
- Feldman, W.C., Mellon, M.T., Gasnault, O., Diez, B., Elphic, R.C., Hagerty, J.J., Lawrence, D.J., Maurice, S., Prettyman, T.H., 2007. Vertical distribution of hydrogen at high northern latitudes on Mars: The Mars Odyssey Neutron Spectrometer. *Geophys. Res. Lett.*, 34. doi:10.1029/2006GL028936.
- Fischer, E.M., Pieters, C.M., 1993. The continuum slope of Mars: Bidirectional reflectance investigations and applications to Olympus Mons. *Icarus* 102, 185–202.
- Fisher, D.A., 2005. A process to make massive ice in the martian regolith using long-term diffusion and thermal cracking. *Icarus* 179, 387–397.
- Fouchet, T., and 10 colleagues, 2007. Martian water vapor: Mars Express PFS/LW observations. *Icarus* 190, 32–49.
- Haberle, R.M., Jakosky, B.M., 1991. Atmospheric effects on the remote determination of thermal inertia on Mars. *Icarus* 90, 187–204.
- Hecht, M.H., 2002. Metastability of liquid water on Mars. *Icarus* 156, 373–386.
- Hess, S.L., Henry, R.M., Leovy, C.B., Ryan, J.A., Tillman, J.E., Chamberlain, T.E., 1976. Preliminary meteorological results on Mars from the Viking 1 lander. *Science* 193, 788–791.
- Hess, S.L., Henry, R.M., Leovy, C.B., Ryan, J.A., Tillman, J.E., 1977. Meteorological results from the surface of Mars: Viking 1 and 2. *J. Geophys. Res.* 82, 4559–4574.
- Holstein-Rathlou, C., Gunnlaugsson, H.P., Merrison, J., Taylor, P., Lange, C., Davis, J., Lemmon, M., and the Phoenix Science Team, 2009. Winds at the Mars Phoenix landing site. *Lunar Planet. Sci. XL* (Abstract 1548).
- Hudson, T.L., Aharonson, O., Schorghofer, N., Farmer, C.B., Hecht, M.H., Bridges, N.T., 2007. Water vapor diffusion in Mars subsurface environments. *J. Geophys. Res.* 112, E05016. doi:10.1029/2006JE002815.
- Hudson, T.L., Zent, A., Hecht, M.H., Wood, S., Cobos, D., 2009. Near-surface humidity at the Phoenix landing site as measured by the Thermal and Electrical Conductivity Probe (TECP). *Lunar Planet. Sci. XL* (Abstract 1804).
- Incropera, F.P., de Witt, D.P., 1985. *Introduction to Heat Transfer*. John Wiley & Sons, New York.
- Ingersoll, A.P., 1970. Mars: Occurrence of liquid water. *Science* 168, 972–973.
- Ivanov, A.B., Muhleman, D.O., 2000. The role of sublimation for the formation of the northern ice cap: Results from the Mars Orbiter Laser Altimeter. *Icarus* 144, 436–448.
- Kieffer, H.H., 1990. H₂O grain size and the amount of dust in Mars' residual north polar cap. *J. Geophys. Res.* 95, 1481–1493.
- Kieffer, H.H., Martin, T.Z., Peterfreund, A.R., Jakosky, B.M., Miner, E.D., Palluconi, F.D., 1977. Thermal and albedo mapping of Mars during the Viking Primary Mission. *J. Geophys. Res.* 82, 4249–4291.
- Koschny, D., Grün, E., 2001. Impacts into ice-silicate mixtures: Crater morphologies, volumes, depth-to-diameter ratios, and yield. *Icarus* 154, 391–401.
- Kreslavsky, M.A., 2009. Dynamic landscapes at high latitudes on Mars: Constraints from populations of small craters. *Lunar Planet. Sci. XL* (Abstract 2311).
- Lefort, A., Russell, P.S., Thomas, N., McEwen, A.S., Dundas, C.M., Kirk, R.L., 2009. Observations of periglacial landforms in Utopia Planitia with the High Resolution Imaging Science Experiment (HiRISE). *J. Geophys. Res.* 114, E04005. doi:10.1029/2008JE003264.
- Malin, M.C., and 13 colleagues, 2007. Context Camera investigation on board the Mars Reconnaissance Orbiter. *J. Geophys. Res.* 112, E05S04. doi:10.1029/2006JE002808.
- McEwen, A.S., and 14 colleagues, 2007. Mars Reconnaissance Orbiter's High Resolution Imaging Science Experiment (HiRISE). *J. Geophys. Res.* 112, E05S07. doi:10.1029/2005JE002605.
- Mellon, M.T., Jakosky, B.M., 1993. Geographic variations in the thermal and diffusive stability of ground ice on Mars. *J. Geophys. Res.* 98, 3345–3364.
- Mellon, M.T., Feldman, W.C., Prettyman, T.H., 2004. The presence and stability of ground ice in the southern hemisphere of Mars. *Icarus* 169, 324–340.
- Mellon, M.T., Boynton, W.V., Feldman, W.C., Arvidson, R.E., Titus, T.N., Bandfield, J.L., Putzig, N.E., Sizemore, H.G., 2008. A prelanding assessment of the ice table depth and ground ice characteristics in martian permafrost at the Phoenix landing site. *J. Geophys. Res.* 113, E00A25. doi:10.1029/2007JE003067.
- Melosh, H.J., 1989. *Impact Cratering: A Geologic Process*. Oxford University Press, New York.
- Miller, R.D., Black, P.B., 2003. Redistribution of water in terrestrial soils at subfreezing temperatures: A review of processes and their potential relevance to Mars. *J. Geophys. Res.* 108 (E4). doi:10.1029/2002JE001873.
- Mills, A.F., 2001. *Mass Transfer*. Prentice Hall, New Jersey.
- Moore, H.J., Hutton, R.E., Scott, R.F., Spitzer, C.R., Shorthill, R.W., 1977. Surface materials of the Viking landing sites. *J. Geophys. Res.* 82, 4497–4523.
- Moore, H.J., Hutton, R.E., Clow, G.D., Spitzer, C.R., 1987. Physical properties of the surface materials at the Viking landing sites on Mars. *US Geol. Survey Prof. Paper* 1389, Washington.
- Morgenstern, A., Hauber, E., Reiss, D., van Gesselt, S., Grosse, G., Schirrmeyer, L., 2007. Deposition and degradation of a volatile-rich layer in Utopia Planitia and implications for the climate history on Mars. *J. Geophys. Res.* 112, E06010. doi:10.1029/2006JE002869.
- Morris, R.V., Graff, T.G., Shelfer, T.D., Bell, J.F., 2001. Effects of palagonitic dust coatings on visible, near-IR, and Mössbauer spectra of rocks and minerals: Implications for mineralogical remote sensing. *Lunar Planet. Sci. XXXII* (Abstract 1912).
- Paterson, W.S.B., 1994. *The Physics of Glaciers*, third ed. Butterworth Heinemann, Oxford.
- Putzig, N.E., Mellon, M.T., 2007. Apparent thermal inertia and the surface heterogeneity of Mars. *Icarus* 191, 68–94. doi:10.1029/j.icarus.2007.05.13.
- Rempel, A.W., 2007. Formation of ice lenses and frost heave. *J. Geophys. Res.* 112. doi:10.1029/2006JF000525.
- Reufer, A., Benz, W., Byrne, S., Searls, M., Thomas, N., Bray, V., McEwen, A., Dundas, C., 2009. Modeling of ice-filled craters at mid-northern latitudes on Mars. *EGU General Assembly* (Abstract 9059).
- Safaieinili, A., Holt, J., Plaut, J., Posiolova, L., Phillips, R., Head, J.W., Seu, R., and SHARAD Team, 2009. New radar evidence for glaciers in Mars Phlegra Montes region. *Lunar Planet. Sci. XL* (Abstract 1988).
- Schofield, J.T., Barnes, J.R., Crisp, D., Haberle, R.M., Larsen, S., Magalhaes, J.A., Murphy, J.R., Seiff, A., Wilson, G., 1997. The Mars Pathfinder Atmospheric Structure Investigation/Meteorology (ASI/MET) experiment. *Science* 278, 1752–1758.
- Schorghofer, N., Aharonson, O., 2005. Stability and exchange of subsurface ice on Mars. *J. Geophys. Res.* 110, E05003. doi:10.1029/2004JE002350.

- Schorghofer, N., Edgett, K.S., 2006. Seasonal surface frost at low latitudes on Mars. *Icarus* 180, 321–334.
- Smith, M.D., 2002. The annual cycle of water vapor on Mars as observed by the Thermal Emission Spectrometer. *J. Geophys. Res.* 107, E11. doi:10.1029/2001JE001522.
- Smith, M.D., Pearl, J.C., Conrath, B.J., Christensen, P.R., 2001. One martian year of atmospheric observations by the Thermal Emission Spectrometer. *Geophys. Res. Lett.* 28, 4263–4266.
- Smith, P.H., and 35 colleagues, 2009. H₂O at the Phoenix landing site. *Science* 325, 58–61.
- Taylor, P.A., Baibakov, K., Brown, S., Hecht, M.H., Hudson, T.L., Li, P.-Y., Lange, C.F., Prieto, L., Savelyev, S., 2006. On the sublimation of ice particles on the surface of Mars: With applications to the 2007/08 Phoenix Scout mission. *Icarus* 181, 375–387.
- Toon, O.B., Pollack, J.B., Ward, W., Burns, J., Bilski, K., 1980. The astronomical theory of climate change on Mars. *Icarus* 44, 552–607.
- Wallace, D., Sagan, C., 1979. Evaporation of ice in planetary atmospheres: Ice-covered rivers on Mars. *Icarus* 39, 385–400.
- Williams, K.E., Toon, O.B., Heldmann, J.L., McKay, C., Mellon, M.T., 2008. Stability of mid-latitude snowpacks on Mars. *Icarus* 196, 565–577.
- Zent, A.P., Hudson, T.L., Hecht, M.H., Cobos, D., Wood, S.E., 2009. Mars regolith thermal and electrical properties: Initial results of the Phoenix Thermal and Electrical Conductivity Probe (TECP). *Lunar Planet. Sci.* XL (Abstract 1125).